Minimizing OCT quantification error via a surface-tracking imaging probe

HYEON-CHEOL PARK,[1] ⓘ ANG LI,[1] ⓘ HONGHUA GUAN,[2] CHETAN BETTEGOWDA,[3] KAISORN CHAICHANA,[4] ALFREDO QUIÑONES-HINOJOSA,[4] AND XINGDE LI[1,2,*]

[1]*Department of Biomedical Engineering, Johns Hopkins University, Baltimore, MD 21215, USA*
[2]*Department of Electrical and Computer Engineering, Johns Hopkins University, Baltimore, MD 21218, USA*
[3]*Department of Neurosurgery, Johns Hopkins School of Medicine, Baltimore, MD 21287, USA*
[4]*Department of Neurologic Surgery, Mayo Clinic, Jacksonville, FL 32224, USA*
[*]*xingde@jhu.edu*

Abstract: OCT-based quantitative tissue optical properties imaging is a promising technique for intraoperative brain cancer assessment. The attenuation coefficient analysis relies on the depth-dependent OCT intensity profile, thus sensitive to tissue surface positions relative to the imaging beam focus. However, it is almost impossible to maintain a steady tissue surface during intraoperative imaging due to the patient's arterial pulsation and breathing, the operator's motion, and the complex tissue surface geometry of the surgical cavity. In this work, we developed an intraoperative OCT imaging probe with a surface-tracking function to minimize the quantification errors in optical attenuation due to the tissue surface position variations. A compact OCT imaging probe was designed and engineered to have a long working distance of ∼ 41 mm and a large field of view of $4 \times 4 \, \text{mm}^2$ while keeping the probe diameter small (9 mm) to maximize clinical versatility. A piezo-based linear motor was integrated with the imaging probe and controlled based upon real-time feedback of tissue surface position inferred from OCT images. A GPU-assisted parallel processing algorithm was implemented, enabling detection and tracking of tissue surface in real-time and successfully suppressing more than 90% of the typical physiologically induced motion range. The surface-tracking intraoperative OCT imaging probe could maintain a steady beam focus inside the target tissue regardless of the surface geometry or physiological motions and enabled to obtain tissue optical attenuation reliably for assessing brain cancer margins in challenging intraoperative settings.

1. Introduction

Brain cancer is one of the most fatal diseases. The five-year survival rate of glioblastoma, the most common form of primary malignant brain cancers, is only 7.2%, with a median survival time of 8 months. Around 18,000 new cases are diagnosed every year in the US alone, and the total number of cases is much higher (more than 80,000 new cases are diagnosed every year) if including other types of non-malignant cancers [1]. In most brain cancer cases, surgery is the first-line therapy, and safely maximizing the extent of the resection is the key to preventing cancer recurrence, minimizing collateral damage to healthy tissues, and prolonging survival [2–4]. However, assessing cancer margins intraoperatively is very challenging, especially in the infiltrative zones, and often resulted in suboptimal surgical outcomes [5–6]. Several technological advances have contributed to accessing cancer margins intraoperatively, such as intraoperative magnetic resonance imaging (iMRI), intraoperative computed tomography (iCT) or ultrasound, Raman spectroscopy or imaging, and fluorescence-guided surgery, but significant challenges remain [7–17]. These imaging technologies have limitations in resolution, field of view (FOV), and more critically in their capability to provide continuous guidance or sufficient specificity to

cancer tissues. On the other hand, OCT has attracted increasing interest for intraoperative brain cancer detection owing to its capability to provide high-resolution, real-time, and continuous guidance without interfering with surgical procedures. More importantly, OCT can provide quantitative feedback to surgeons with a few millimeters of imaging depth and a FOV comparable with the size of the tissue surgeons need to take out near the cancer margins [18]. The optical attenuation coefficient, a quantitative parameter of tissue property, which can be extracted from OCT signals, has been recognized as a viable metric for classifying pathological changes [19–25]. For example, cancerous brain tissues have a relatively low optical attenuation coefficient (*i.e.*, OCT signal decays slowly) compared to non-cancerous white matter, which have a higher attenuation coefficient (*i.e.*, OCT signal decays more rapidly) [24–27]. Our group recently demonstrated a quantitative OCT technique for differentiating cancer and non-cancer in human brain tissues [25]. We found an optimal attenuation threshold and generated real-time color-coded attenuation map to provide direct visual guidance during brain cancer surgery. The result showed over 80% specificity and 100% sensitivity for glioblastoma, demonstrating a highly promising potential of the quantitative OCT for intraoperative guidance of surgical interventions. For intraoperative use of the quantitative OCT technology, precise, reliable, and real-time attenuation mapping is essential. The recently developed Fourier-domain method affords fast, robust, and accurate attenuation coefficient calculation and does not require explicit information on tissue surface position [28], while the beam profile inside the tissue still needs to be carefully compensated by using reference measurements from a tissue phantom of known optical properties to extract accurate tissue attenuation coefficient from the depth-dependent OCT intensity profile. Several methods have been used to compensate the beam profile, including normalizing OCT signal profiles by a reference one (e.g., a theoretical point spread function (PSF) or a measured PSF from a reference phantom, taken at the same focus position as inside the tissue) [28–32]. However, it is extremely challenging to maintain a steady focus position during surgery due to the patient's arterial pulsation and breathing, the operator's motion, and the complex tissue surface geometry of the surgical cavity. Theoretical or reference PSF needs to be actively adjusted with respect to the imaging beam focus positions in tissue, which requires significant computational power. Moreover, in real-world situations, the OCT images can often go out of focus or even flip when the tissue moves more than the imaging depth, which hinders accurate quantification of tissue optical attenuation coefficient. One potential solution to these challenges is to implement a scheme that can reliably maintain the tissue surface position relative to the imaging probe during real-time OCT imaging [33].

This work reports a surface-tracking OCT imaging probe to maintain a stable tissue surface position relative to the imaging probe for intraoperative brain cancer detection. A compact OCT imaging probe with a long working distance (41 mm), small diameter (9 mm), and a large FOV (4×4 mm^2) was designed and engineered to access deep lesions through the surgical cavities without interfering with surgical procedures. A piezo-based, fast-response linear motor was also integrated with the OCT imaging probe and feedback-controlled to move the probe and maintain a constant probe-tissue surface separation based upon the tissue surface position inferred from OCT images in real-time. OCT imaging can provide a sufficient imaging speed with high resolution for accurate surface tracking, and real-time surface detection was implemented by using a graphic processing unit (GPU). The surface tracking performance of the probe was tested by imaging a physically oscillating sample mimicking the physiological brain motions during surgery. It was found that the surface tracking-enabled probe could suppress more than 90% of the typical brain motion amplitude, demonstrating its capability to obtain a reliable attenuation map in clinical settings.

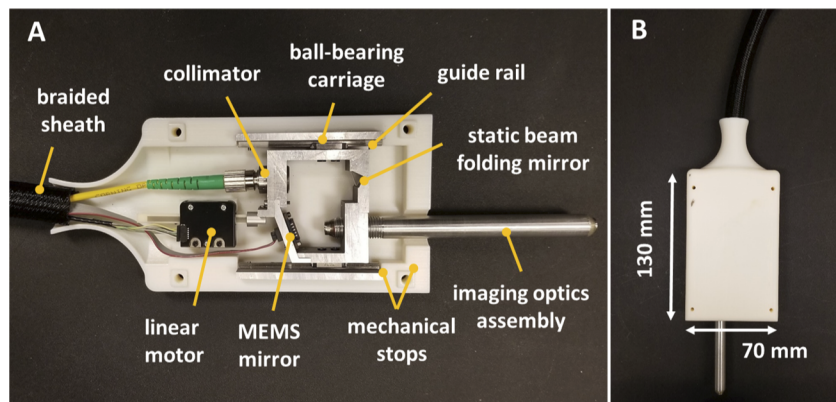## 2. Intraoperative OCT imaging probe capable of surface tracking

For clinical versatility, the imaging probe needs to have a long working distance and a large FOV while keeping the probe diameter as small as possible, especially for accessing deep lesions through the surgical cavity. However, it is challenging to achieve such requirements with off-the-shelf lenses of a small diameter and a conventional 4f optical layout due to the off-axis aberrations. It often requires a specialized optical design with multiple elements to achieve a good telecentricity. In this work, we implemented a simple and cost-effective design using off-the-shelf lenses. Figure 1 shows the optical layout and ray-tracing simulation results. The light delivered by a fiber was collimated and scanned by a two-dimensional (2D) microelectromechanical system (MEMS) scanning mirror, then focused by an imaging optics assembly. The assembly consists of three achromatic doublets of a 6 mm diameter. The first two identical lenses, each with a focal length of 30 mm, were separated by 40 mm, smaller than 2f, resulting in a slightly diverging beam after the second lens (dotted red box in Fig. 1(A)). The last focusing lens with a focal length of 25 mm (f_3) was then positioned at the converging point of the scanned beams to minimize off-axis aberrations (dotted purple box in Fig. 1(A)). The ray-tracing result shows that a diffraction-limited resolution of ∼ 30 μm can be achieved over a large FOV of ∼ 4 × 4 mm² (at ±2 deg mechanical scanning angle of the MEMS mirror) with a long working distance of ∼ 41 mm. The imaging beam is non-telecentric with a maximum focal shift of less than 200 μm across the entire FOV. The imaging beam is non-telecentric, and there could be some aberrations such as spherical and coma at the edge of the FOV with non-customized optics. However, the slightly curved image plane (less than 200 μm across the entire FOV) and aberrations were tolerable for attenuation quantification for the brain cancer detection. We averaged OCT signals over ∼ 300 μm of FOV along the lateral direction for minimizing speckle noises, followed by compensating the beam profile using a reference phantom.
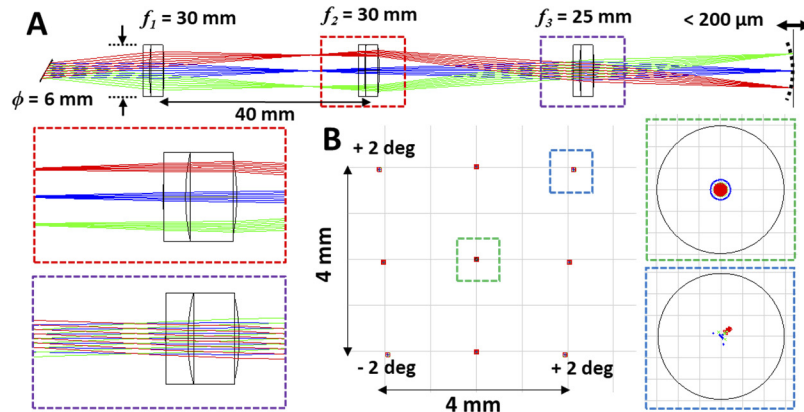
Fig. 1. (A) Optical layout of the surface tracking intraoperative imaging probe with a MEMS scanning mirror and three achromatic doublets (6 mm in diameter). Different from a conventional relay optics layout, the first two lenses were separated by 40 mm, which is less than the sum of the focal lengths, resulting in a slightly diverging beam. In addition, the last focusing lens was placed at the converging point of the scanned beams. (B) Ray-tracing simulation results of the optical layout. Diffraction-limited and near-telecentric performances were achieved over a large FOV of ∼ 4 × 4 mm² with a long working distance of ∼ 41 mm.

Figures 2(A) and (B) show photographs of the surface tracking imaging probe assembly, which consists of a compact OCT imaging module (with the optical design shown in Fig. 1(A)) and a linear motor for surface tracking. OCT imaging module includes a fiber-optic collimator, a MEMS scanning mirror, and an imaging optics assembly consisting of three achromatic doublets.

The achromatic lenses were inserted inside a metal tube with a 9 mm outer diameter, and the precise spacing between the lenses was secured by spacers of the desired length between adjacent lenses. The fiber-optic collimator, MEMS scanner, and the imaging optics assembly were secured inside aluminum housing with threads. An additional static beam folding mirror was also placed between the collimating lens and the MEMS scanning mirror so that the optical fiber and the imaging probe can both be along the forward-looking direction, which is more convenient for intraoperative use. The imaging probe was then integrated with a PZT based linear motor (PiezoMotor, LL06) for surface tracking. The PZT based motor provides a very compact footprint (23.4 mm x 19.6 mm x 10.35 mm (W x H x D)) with a fast response time and enough force (6.5 N stall force) to move the OCT imaging probe. The linear motor provides a maximum travel range of 70 mm with a step resolution of 4 μm and a maximum stepping rate of 2.5 kHz that corresponds to a maximum speed of 10 mm/s. The fast-stepping rate of this PZT motor enabled to compensate physiological motions or the surgeon's tremor [34]. The linear motor was controlled by an external motor driver (PMD301) designed to work in a closed-loop with real-time feedback from an integrated position sensor (encoder). The aluminum housing of the imaging module was connected with the linear motor and mounted inside a 3D printed plastic enclosure with two linear guide rails and ball-bearing carriages attached on the sidewalls of the housing. The guide rails with carriages prevented lateral displacement and secured motion along the longitudinal direction of the imaging probe during surface tracking. Mechanical stops on the enclosure ensured safety during the surface tracking. The optical fiber was protected inside the 3 mm diameter furcation tubing consisting of a 900 μm diameter inner fiber tubing, Kevlar protective threads, and a PVC outer jacket to prevent the fiber from breaking during surface tracking when the fiber moved with the probe. In addition, the optical fiber and all the electrical drive/control wires for the motor and the MEMS scanning mirror were further protected inside a braided sheath. The overall dimension of the probe enclosure is 70 mm x 130 mm x 30 mm (W x H x D) and can be held by either an operator's hand or a mechanical arm.

Fig. 2. (A) Photograph of the surface tracking intraoperative imaging probe assembly. The probe is composed of a compact OCT imaging probe module connected with a linear motor for surface tracking. Additional guide rails with ball-bearing carriages were installed to guide the motion along a line. (B) Photograph of a fully assembled probe. The overall dimensions are 70 mm x 130 mm x 30 mm (W x H x D), and the optical fiber and the drive/control wires were further protected inside a braided sheath.

The probe was then integrated with an OCT imaging system. The details of our OCT imaging system have been reported elsewhere [35]. In brief, the system consists of a vertical-cavity surface-emitting laser (VCSEL) swept light source and fiber-optic Mach-Zehnder interferometer. The VCSEL provided a 100 kHz A-line scan rate at the central wavelength of 1310 nm with a 3

dB spectral bandwidth of ~ 90 nm (10 dB bandwidth of ~ 110 nm). The VCSEL generates an internal linear *k*-clock for an imaging depth up to 6 mm in air, and the clock was used to trigger and synchronize data acquisition with a high-speed digitizer. A green aiming laser at 532 nm was also coupled into the probe with a fiber-optic wavelength division multiplexer (WDM) to provide visual guidance of an imaging area during intraoperative use. The axial resolution was measured to ~ 9 μm in air, the detection sensitivity and the signal roll-off of the system were measured to be better than -115 dB and -0.6 dB/mm, respectively.

3.   Real-time surface detection and tracking

Real-time surface detection and feedback control of the motor were realized by using a GPU-accelerated OCT data processing and display framework, including a maximum-gradient based fast surface detection algorithm implemented with CUDA C++. Figure 3(A) illustrates the software architecture comprising three threads, namely, the acquisition, processing, and motor control threads. The acquisition thread controls data acquisition and ensures the synchronization between the MEMS mirror scanning and the data digitization/acquisition. Whenever a fresh B-frame is acquired by the digitizer, the acquisition thread alerts the processing thread and triggers data transfer from the host memory (central processing unit, CPU) to the device memory (GPU). The processing thread controls the host-device data transfer and the GPU data processing. It launches two separate streams in the GPU, one being the copy stream, the other being the processing stream. In this way, the data transfer and processing take place concurrently in a pipelined fashion. The copy stream copies the fresh sample data from the host to the device memory. Simultaneously, the process stream accesses the device memory where the previous batch of data is stored, then performs a series of operations, including fast Fourier transform (FFT), magnitude computation, and surface detection. The processed data is then rendered and displayed. Once a B-frame image was processed, the motor control thread took the detected current surface position and compared it with a preset target location. Then commands for compensating error between the current surface position and the target position were sent to the motor controller through a USB serial communication interface (virtual COM port). The motor controller moved the motor to a target position in a closed-loop, which runs every 1 ms with encoder feedback. While the motor was moving, the target position could be continuously updated with the refresh rate same as the imaging frame rate.

The key to real-time surface detection and tracking is the implementation of a fast surface detection algorithm. The algorithm needs to be simple and robust, as well as parallelizable (so it can be executed via GPU). We implemented a maximum-gradient algorithm to identify the tissue surface: a backward differentiation is first applied to each A-line to compute the gradient, then the peak gradient location is considered as the surface location within the A-line. A parallel reduction algorithm was utilized to speed up peak detection within each A-line [36], which drastically reduced the time complexity of the peak finding process from $O(n)$ to $O(log(n))$. The peak locations of all the A-lines in a B-frame were found independently in parallel and then averaged as the surface location of the current B-frame. The overall B-frame processing time (including surface detection) was benchmarked with a frame sized to 1728×512 (axial x lateral) pixels at ~180 frames/sec imaging speed on a desktop computer equipped with an Intel Core i7-2600k CPU and an Nvidia GTX 1060 GPU. As shown in GPU profiling results in Fig. 3(B), a B-frame image was processed within 340 μs, including merely 63 μs used for surface detection, while the overall processing time, including data transfer between the threads, was benchmarked as 1 ms as shown in Fig. 3(B).

Finding all the surface positions in a frame would significantly improve surface detection reliability, particularly under harsh intra-operative imaging conditions. For example, diluted blood during surgical procedures may induce some spurious high back reflections or reduce the signal-to-noise ratio due to increased attenuation by the blood. When the back-reflected signal
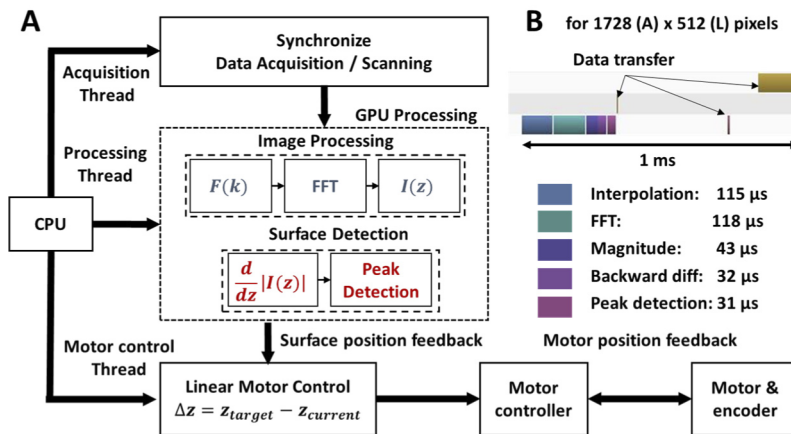
Fig. 3. (A) Software architecture for the surface tracking probe. GPU-accelerated OCT data processing was used for real-time surface detection and feedback control of the motor. (B) Benchmarks of GPU processing of a B-frame image with 1728×512 pixels captured at ~180 frames per second. Overall processing time was benchmarked as ~ 1 ms, including data transfer between threads and the image processing. A B-frame image was processed within 340 µs, including 63 µs dedicated to surface detection. The parallel computing using GPU drastically reduced the time complexity of the peak finding process and realized real-time surface detection and tracking.

is high and saturates the detector, the surface detection algorithm returns the first pixel of the image as a surface position since the highest peak is DC component of the Fourier transform. On the other hand, when the signal is very noisy, the surface detection algorithm returns a static background peak located at around one-fourth of the imaging depth from internal back reflections of the interferometer. A static artificial peak can also be created intentionally by adding a thin glass window at the distal end of an imaging probe. Back-reflected lights from both glass window surfaces would create a self-interference static peak near the top of the OCT image. This artificial peak would be barely distinguishable on the OCT image, but it can be easily removed and won't affect the quantification of the tissue optical attenuation. Nevertheless, these faulty surface detections can be effectively mitigated by averaging the surface positions for all A-lines within a B-frame. Moreover, the surface of the surgical tissue bed may not be flat and can often have complex geometry. It is a reasonable and safe compromise to place the probe based on an averaged surface position. To further ensure safety during intraoperative usage of surface tracking, position limit settings were also implemented in the software. If the detected surface position exceeds the top or bottom of the OCT image due to some abrupt relative motions between the probe and tissue surface, which are too fast to follow, the software automatically disables surface tracking.

4. Results

The motion tracking performance of the imaging probe was systematically investigated. At first, a sample IR card was placed 4 mm away from the target position, and the surface tracking function was enabled. Figure 4(A) shows the recorded surface position change. The probe immediately moved to a target position at the maximum speed of the motor, 10 mm/s, as the surface tracking enabled. No significant overshooting was found, and it took an additional ~ 30 ms to be stabilized with a minor fluctuation of less than 10 µm, as shown in the inset image of Fig. 4(A).

The dynamic motion tracking performances were also characterized by imaging a physically oscillating sample. An IR card was placed at the end of a lever attached to a galvanometer scanner,
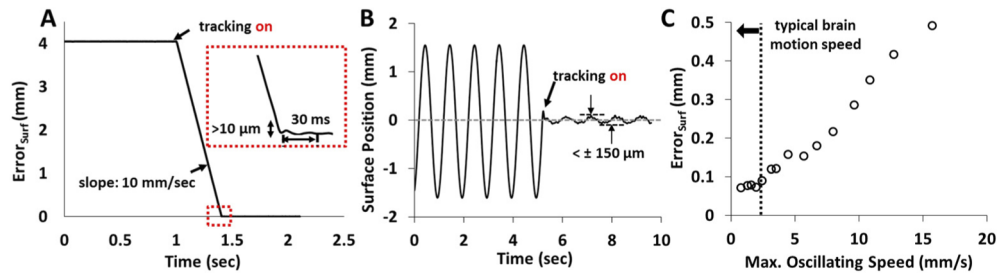
Fig. 4. Surface tracking performance of the imaging probe. (A) Step response; the probe immediately compensated the surface position error with the maximum speed of the motor without significant overshooting. (B) Dynamic response measured with an oscillating sample surface at 1 Hz; the probe successfully suppressed over 90% of the total surface motion. (C) Maximum surface position error with respect to the sample surface oscillating speed; within a typical brain physiological motion speed range, the probe can suppress the error to less than 0.1 mm.

and the scanner was oscillated to mimic physiological motions (0.5–2 Hz). Figure 4(B) shows a recorded surface trajectory when the sample oscillates ±1.5 mm at 1 Hz, which corresponds to the maximum movement speed of ∼ 9.4 mm/s ($2 \cdot \pi \cdot f \cdot A$, where f is the frequency of the oscillation, and A is the amplitude). The real-time surface position feedback from OCT imaging and the fast response of the PZT based motor successfully suppressed over 90% of the maximum motion in real-time, while some residual position errors were remained mainly due to the time delays associated with image processing (per frame) and communication between the software and the motor (typically < 1 ms). Figure 4(C) shows the maximum surface position error with respect to the maximum movement speed. At the velocity range of the typical brain motion, 0 - 2 mm/s [37], the surface tracking probe can sufficiently suppress dynamic motions to within an error of less than 0.1 mm. Even in some extreme cases where the movement speed exceeded the motor's maximum speed, we were still able to suppress the majority of the motions down to a few hundred microns. The results clearly demonstrated that the probe could reliably maintain a beam focus position inside the target tissue regardless of the physiological motions or any physical interferences, such as the surgeon's hand motion. Thus, it can minimize quantification errors of the tissue optical attenuation coefficient.

The surface tracking performance of the probe was further demonstrated by imaging actual physiological motions of a rat chest in vivo. All the animal housing and experimentation procedures were performed under the standards of humane animal care described in the National Institutes of Health Guide for the Care and Use of Laboratory Animals with protocols approved by the Institutional Animal Care and Use Committee at the Johns Hopkins University. During imaging, the rat was anesthetized and placed on a regulated heating pad (37 °C) with the body restrained by a customized holder. The inhalation isoflurane anesthesia was used (4% for induction, 1% - 2% for maintenance, in 0.5 L/min oxygen). After imaging, the isoflurane anesthesia was removed while the heating pad support continued until the rat fully recovered. We imaged the chest area of a rat where it had the maximum movement range due to breathing (Fig. 5(A)). Figures 5(B) and (C) show representative real-time OCT images captured with the probe without (Fig. 5(B), Visualization 2) and with (Fig. 5(C), Visualization 3) surface tracking. Figure 5(D) shows the recorded surface position without (top plot) and with (bottom plot) surface tracking. As shown in Fig. 5(D), the surface position rapidly changed, especially at exhale, and exhibited an abrupt motion that represents some extreme cases. The measured motion speed was ∼ 8.6 mm/s during inhale and ∼ 17.6 mm/s during exhale. Clearly, the exhale motion speed exceeded the motor speed limit, resulting in a large tracking difference (∼500 μm).

When the surface tracking function was enabled, the probe spontaneously followed the surface to compensate movements, and we were able to maintain reliable tissue surface positions within a range of less than 200 μm during inhale and less than 500 μm during exhale.
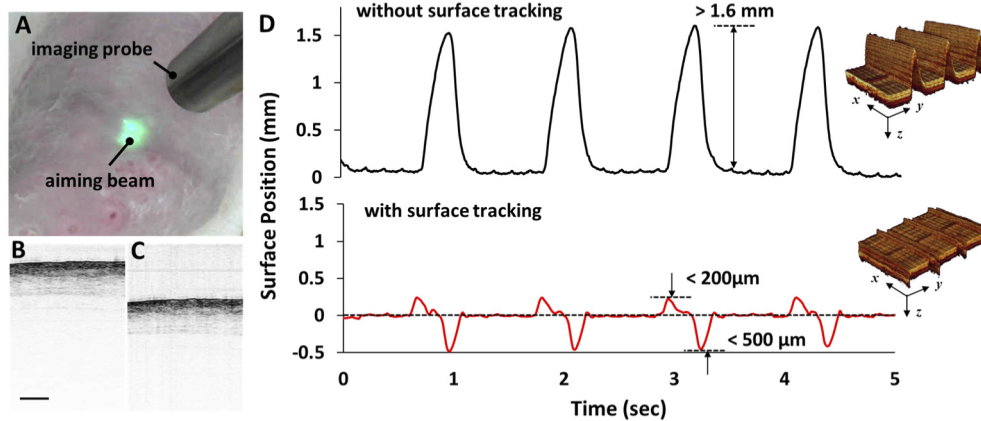

Fig. 5. (A) Visualization 1; The surface-tracking probe simultaneously followed the rat chest motion due to breathing when the surface tracking was enabled. Green aiming laser indicates the imaging area. (B-C) Visualization 2 and Visualization 3; Recorded real-time OCT images of the rat chest during breathing without (B) and with (C) surface tracking. (D) Recorded surface position changes with and without surface tracking. The inset images show reconstructed 3D images with 512 consecutive B-frame images. Scale bar: 1 mm.

Finally, the capability of the surface tracking probe for intraoperative brain cancer detection was further validated by analyzing quantification errors in optical attenuation due to the surface position changes. Figure 6(A) shows a measured influence of the surface position error on tissue optical attenuation coefficient with surgically removed fresh human brain tissue samples obtained at the Johns Hopkins Hospital under an approved Institutional Review Board protocol. The attenuation coefficient was calculated by the Fourier-domain method described in Ref. [28]. The influences of the depth-dependent effects of the beam profiles, including the field curvature during the lateral beam scanning, were compensated with silicon phantom data with a known attenuation coefficient [29]. The phantom data/images were collected at various focus positions before tissue imaging, and the OCT signals from the tissue sample were normalized with the OCT signals from the phantom taken at the same lateral scanning location and focal position. As shown in Fig. 6(A), a consistent tissue optical attenuation coefficient could be extracted with a less than $0.1\,\text{mm}^{-1}$ error if the surface position error is kept within $500\,\mu\text{m}$. As the surface position varied further from the initial position, the error in optical attenuation became significant due to the mismatch between the imaging beam profile and the reference PSF, as well as the reduced signal-to-noise ratio associated with the out-of-focused OCT signals. We investigated the effect of these quantification errors on sensitivity or specificity to distinguish cancer and non-cancer tissues. We quantified optical attenuation coefficients from OCT images of 15 human brain tissues (11 cancer and 4 non-cancer). The attenuation threshold value was set to maximize both sensitivity and specificity, and we achieved ~83% of both sensitivity and specificity. Then, we randomly added given errors (caused by tissue surface variations) to the optical attenuation data. These errors broadened the statistical distribution of the optical attenuation coefficients and altered the sensitivity and specificity at the given threshold. Figure 6(B) shows that we could still minimize sensitivity or specificity change less than 1% if the attenuation coefficient error is less than $0.1\,\text{mm}^{-1}$, which corresponds to a maximum surface position variation of ~$500\,\mu\text{m}$ (Fig. 6(A)). The results indicate that the as-developed surface tracking probe can reliably obtain

an accurate tissue optical attenuation coefficient and maximize the outcome of the quantitative OCT in challenging intraoperative settings.
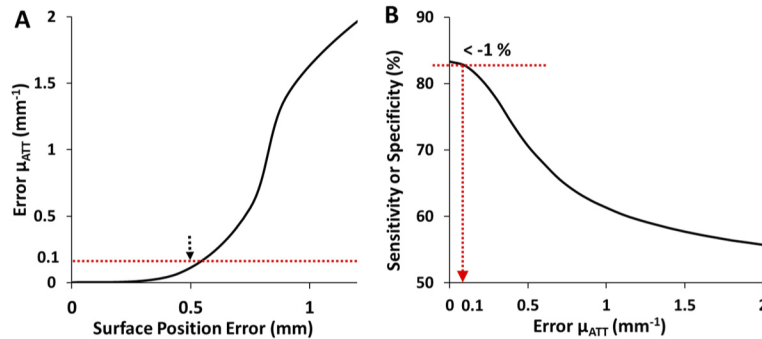
Fig. 6. (A) Measured optical attenuation coefficient error versus tissue surface position error. (B) Sensitivity or specificity reduces as the quantification error of the optical attenuation coefficient increases. An ~ 0.5 mm of surface position error induced an optical attenuation coefficient error of ~ 0.1 mm^{-1} and reduced sensitivity or specificity by $\sim 1\%$ (as indicated by the red dashed lines).

5. Conclusion and discussion

We developed and demonstrated a surface tracking imaging probe for quantitative intraoperative OCT imaging. The probe provides a long working distance of ~ 41 mm and a large FOV of 4×4 mm^2 with a small probe diameter of 9 mm, making it easier to access deeper lesions without interfering with any surgical procedures. A GPU accelerated parallel processing implementation enabled detection of the surface positions of all A-lines within any given B-frame image without delaying other tasks and contributed to improving the surface detection reliability and speed, especially when imaging an area of complex tissue morphologies. Real-time OCT imaging and surface detection provided rapid position feedback, and the fast-response PZT based linear motor successfully followed the tissue surface movement and maintained a reliable focus position inside the target tissue. The performance of the surface tracking probe was characterized by imaging a physically oscillating sample at different speeds. Within a typical physiological brain motion speed range, the probe could maintain stable tissue surface positions with an accuracy of 0.1 mm from the target position. Even in some extreme cases where the surface moved much faster than normal physiological motion or near the maximum speed of the motor, the probe was still able to suppress the majority of the surface variations, sufficient to obtain reliable optical attenuation property (see Fig. 6). We believe that the surface tracking performance can be further optimized by implementing an advanced PID control in the future. In addition, both mechanical stops and software tracking limits are used to further ensure the safety during intraoperative use of surface tracking to avoid unsafe, large movement of the probe towards the tissue. The as-developed surface tracking intraoperative OCT imaging probe can play a valuable role in a clinical translation of quantitative OCT for intraoperative assessment of brain cancer margins.

Disclosures. The authors declare that there are no conflicts of interest related to this article.

References

1. Q. T. Ostrom, N. Patil, G. Cioffi, K. Waite, C. Kruchko, and J. S. Barnholtz-Sloan, "CBTRUS Statistical Report: Primary Brain and Other Central Nervous System Tumors Diagnosed in the United States in 2013–2017", Neuro-Oncol. 22, Supplement 1 (2020).

2. M. Lacroix, D. Abi-Said, D. R. Fourney, Z. L. Gokaslan, W. Shi, F. DeMonte, F. F. Lang, I. E. McCutcheon, S. J. Hassenbusch, E. Holland, K. Hess, C. Michael, D. Miller, and R. Sawaya, "A multivariate analysis of 416 patients with glioblastoma multiforme: Prognosis, extent of resection, and survival," J. Neurosurg. **95**(2), 190–198 (2001).

3. G. E. Keles, K. R. Lamborn, and M. S. Berger, "Low-grade hemispheric gliomas in adults: A critical review of extent of resection as a factor influencing outcome," J. Neurosurg. **95**(5), 735–745 (2001).

4. N. Sanai, M. Y. Polley, M. W. McDermott, A. T. Parsa, and M. S. Berger, "An extent of resection threshold for newly diagnosed glioblastomas," J. Neurosurg. **115**(1), 3–8 (2011).

5. F. K. Albert, M. Forsting, K. Sartor, H.-P. Adams, and S. Kunze, "Early postoperative magnetic resonance imaging after resection of malignant glioma: Objective evaluation of residual tumor and its influence on regrowth and prognosis," Neurosurgery **34**(1), 45–61 (1994).

6. M. J. McGirt, D. Mukherjee, K. L. Chaichana, K. D. Than, J. D. Weingart, and A. Quinones-Hinojosa, "Association of surgically acquired motor and language deficits on overall survival after resection of glioblastoma multiforme," Neurosurgery **65**(3), 463–470; discussion 469–470 (2009).

7. US O. M. Rygh, T. Selbekk, S. H. Torp, S. Lydersen, T. A. N. Hernes, and G. Unsgaard, "Comparison of navigated 3D ultrasound findings with histopathology in subsequent phases of glioblastoma resection," Acta Neurochir. **150**(10), 1033–1042; discussion 1042 (2008).

8. E. Uhl, S. Zausinger, D. Morhard, T. Heigl, B. Scheder, W. Rachinger, C. Schichor, and J.-C. Tonn, "Intraoperative computed tomography with integrated navigation system in a multidisciplinary operating suite," Neurosurgery **64**(2), 231–240; discussion 239–240 (2009).

9. K. Özduman, E. Yıldız, A. Dinçer, A. Sav, and M. N. Pamir, "Using intraoperative dynamic contrast enhanced T1-weighted MRI to identify residual tumor in glioblastoma surgery: Technical note," J. Neurosurg. **120**(1), 60–66 (2014).

10. W. Stummer, U. Pichlmeier, T. Meinel, O. D. Wiestler, F. Zanella, and H. J. Reulen, and ALA-Glioma Study Group, "Fluorescence-guided surgery with 5-aminolevulinic acid for resection of malignant glioma: a randomised controlled multicentre phase III trial," Lancet Oncol. **7**(5), 392–401 (2006).

11. N. Sanai, L. A. Snyder, N. J. Honea, S. W. Coons, J. M. Eschbacher, K. A. Smith, and R. F. Spetzler, "Intraoperative confocal microscopy in the visualization of 5-aminolevulinic acid fluorescence in low-grade gliomas," J. Neurosurg. **115**(4), 740–748 (2011).

12. W. Stummer, J.-C. Tonn, C. Goetz, W. Ullrich, H. Stepp, A. Bink, T. Pietsch, and U. Pichlmeier, "5-Aminolevulinic acid-derived tumor fluorescence: The diagnostic accuracy of visible fluorescence qualities as corroborated by spectrometry and histology and postoperative imaging," Neurosurgery **74**(3), 310–320 (2014).

13. M. Ji, D. A. Orringer, C. W. Freudiger, S. Ramkissoon, X. Liu, D. Lau, A. J. Golby, I. Norton, M. Hayashi, N. Y. Agar, G. S. Young, C. Spino, S. Santagata, S. Camelo-Piragua, K. L. Ligon, O. Sagher, and X. S. Xie, "Rapid, label-free detection of brain tumors with stimulated Raman scattering microscopy," Sci. Transl. Med. **5**(201), 201ra119 (2013).

14. O. Uckermann, R. Galli, S. Tamosaityte, E. Leipnitz, K. D. Geiger, G. Schackert, E. Koch, G. Steiner, and M. Kirsch, "Label-free delineation of brain tumors by coherent anti-stokes Raman scattering microscopy in an orthotopic mouse model and human glioblastoma," PLoS One **9**(9), e107115 (2014).

15. M. Ji, S. Lewis, S. Camelo-Piragua, S. H. Ramkissoon, M. Snuderl, S. Venneti, A. Fisher-Hubbard, M. Garrard, D. Fu, A. C. Wang, J. A. Heth, C. O. Maher, N. Sanai, T. D. Johnson, C. W. Freudiger, O. Sagher, X. S. Xie, and D. A. Orringer, "Detection of human brain tumor infiltration with quantitative stimulated Raman scattering microscopy," Sci. Transl. Med. **7**(309), 309ra163 (2015).

16. M. Jermyn, K. Mok, J. Mercier, J. Desroches, J. Pichette, K. Saint-Arnaud, L. Bernstein, M.-C. Guiot, K. Petrecca, and F. Leblond, "Intraoperative brain cancer detection with Raman spectroscopy in humans," Sci. Transl. Med. **7**(274), 274ra19 (2015).

17. T. Garzon-Muvdi, C. Kut, X. D. Li, and K. L. Chaichana, "Intraoperative imaging techniques for glioma surgery," Future Oncol. **13**(19), 1731–1745 (2017).

18. G. E. Keles, D. A. Lundin, K. R. Lamborn, E. F. Chang, G. Ojemann, and M. S. Berger, "Intraoperative subcortical stimulation mapping for hemispheric perirolandic gliomas located within or adjacent to the descending motor pathways: Evaluation of morbidity and assessment of functional outcome in 294 patients," J. Neurosurg. **100**(3), 369–375 (2004).

19. K. Bizheva, W. Drexler, M. Preusser, A. Stingl, T. Le, H. Budka, A. Unterhuber, B. Hermann, B. Povazay, H. Sattmann, and A. F. Fercher, "Imaging *ex vivo* healthy and pathological human brain tissue with ultra-high-resolution optical coherence tomography," J. Biomed. Opt. **10**(1), 011006 (2005).

20. H. Böhringer, D. Boller, J. Leppert, U. Knopp, E. Lankenau, E. Reusche, G. Hüttmann, and A. Giese, "Time-domain and spectral-domain optical coherence tomography in the analysis of brain tumor tissue," Lasers Surg. Med. **38**(6), 588–597 (2006).

21. H. J. Böhringer, E. Lankenau, F. Stellmacher, E. Reusche, G. Hüttmann, and A. Giese, "Imaging of human brain tumor tissue by near-infrared laser coherence tomography," Acta Neurochir. **151**(5), 507–517; discussion 517 (2009).

22. O. Assayag, K. Grieve, B. Devaux, F. Harms, J. Pallud, F. Chretien, C. Boccara, and P. Varlet, "Imaging of non-tumorous and tumorous human brain tissue with full-field optical coherence tomography," Neuroimage Clin. **2**, 549–557 (2013).

23. M. Almasian, L. S. Wilk, P. R. Bloemen, T. G. van Leeuwen, M. ter Laan, and M. C. G. Aalders, "Pilot feasibility study of *in vivo* intraoperative quantitative optical coherence tomography of human brain tissue during glioma resection," J. Biophotonics **12**(10), e201900037 (2019).

24. R. Juarez-Chambi, C. Kut, J. Rico-Jimenez, K. Chaichana, J. F. Xi, D. Campos-Delgado, F. Rodriguez, A. Quiñones-Hinojosa, X. D. Li, and J. Jo, "AI-Assisted In Situ Detection of Human Glioma Infiltration Using a Novel Computational Method for Optical Coherence Tomography," Clin. Cancer Res. **25**(21), 6329–6338 (2019).

25. C. Kut, K. L. Chaichana, J. Xi, S. M. Raza, X. Ye, E. R. McVeigh, F. J. Rodriguez, A. Quiñones-Hinojosa, and X. D. Li, "Detection of human brain cancer infiltration *ex vivo* and *in vivo* using quantitative optical coherence tomography," Sci. Transl. Med. **7**(292), 292ra100 (2015).

26. E. B. Kiseleva, K. S. Yashin, A. A. Moiseev, M. A. Sirotkina, L. B. Timofeeva, V. V. Fedoseeva, A. I. Alekseeva, I. A. Medyanik, N. N. Karyakin, and L. Ya. Kravets, and N. D. Gladkova, "Cross-Polarization Optical Coherence Tomography in Comparative *in vivo* and *ex vivo* Studies of the Optical Properties of Normal and Tumorous Brain Tissues," Sovrem. Tehnol. Med. **9**(4), 177 (2017).

27. K. S. Yashin, E. B. Kiseleva, A. A. Moiseev, S. S. Kuznetsov, L. B. Timofeeva, N. P. Pavlova, G. V. Gelikonov, I. A. Medyanik, L. Y. Kravets, E. V. Zagaynova, and N. D. Gladkova, "Quantitative nontumorous and tumorous human brain tissue assessment using microstructural co- and cross-polarized optical coherence tomography," Sci. Rep. **9**(1), 2024 (2019).

28. W. Yuan, C. Kut, W. Liang, and X. D. Li, "Robust and fast characterization of OCT-based optical attenuation using a novel frequency-domain algorithm for brain cancer detection," Sci. Rep. **7**(1), 44909 (2017).

29. J. F. Xi, Y. P. Chen, and X. D. Li, "Characterizing optical properties of nano contrast agents by using cross-referencing OCT imaging," Biomed. Opt. Express **4**(6), 842–851 (2013).

30. S. K. Chang and A. Bowden, "Review of methods and applications of attenuation coefficient measurements with optical coherence tomography," J. Biomed. Opt. **24**(9), 1 (2019).

31. P. Gong, M. Almasian, G. van Soest, D. M. de Bruin, T. G. van Leeuwen, D. D. Sampson, and D. J. Faber, "Parametric imaging of attenuation by optical coherence tomography: review of models, methods, and clinical translation," J. Biomed. Opt. **25**(4), 040901 (2020).

32. K. Vermeer, J. Mo, J. Weda, H. Lemij, and J. De Boer, "Depth-resolved model-based reconstruction of attenuation coefficients in optical coherence tomography," Biomed. Opt. Express **5**(1), 322–337 (2014).

33. M. J. Cobb, X. M. Liu, and X. D. Li, "Continuous focus tracking for real-time optical coherence tomography," Opt. Lett. **30**(13), 1680–1682 (2005).

34. C. Song, P. L. Gehlbach, and J. U. Kang, "Active tremor cancellation by a "Smart" handheld vitreoretinal microsurgical tool using swept source optical coherence tomography," Opt. Express **20**(21), 23414–23421 (2012).

35. H.-C. Park, X. Zhang, W. Yuan, L. Zhou, H. Xie, and X. D. Li, "Ultralow-voltage electrothermal MEMS based fiber-optic scanning probe for forward-viewing endoscopic OCT," Opt. Lett. **44**(9), 2232–2235 (2019).

36. M. Harris, "Optimizing parallel reduction in CUDA," Nvidia Develop. Technol. **2**, 70 (2007).

37. D. Greitz, R. Wirestam, A. Franck, B. Nordell, C. Thomsen, and F. Ståhlberg, "Pulsatile brain movement and associated hydrodynamics studied by magnetic resonance phase imaging," Neuroradiology **34**(5), 370–380 (1992).